Role of scan strategies in modulating micro and macro-cracking in CM247LC processed by powder bed fusion–laser beam

Citation for the original published paper (version of record):
Jabir Hussain, A., Schröder, J., Xu, J. et al (2026). Role of scan strategies in modulating micro and macro-cracking in CM247LC processed by powder
bed fusion–laser beam. Progress in Additive Manufacturing, 11(6): 6235-6251.
http://dx.doi.org/10.1007/s40964-026-01701-z

Progress in Additive Manufacturing (2026) 11:6235–6251
https://doi.org/10.1007/s40964-026-01701-z

RESEARCH

Role of scan strategies in modulating micro and macro-cracking in CM247LC processed by powder bed fusion–laser beam

Ahmed Fardan[1] · Jakob Schröder[2] · Jinghao Xu[3] · Håkan Brodin[1,4] · Eduard Hryha[1]

Received: 24 November 2025 / Accepted: 7 April 2026 / Published online: 24 April 2026

Abstract

This study investigates the influence of different scan strategies, specifically scan rotation (0°, 67°, and 90°) and remelting (Double 67° and Double 90°), on the microstructure evolution, residual stress distribution, cracking behavior and mechanical properties of CM247LC superalloy fabricated by powder bed fusion–laser beam (PBF–LB). Scan strategy significantly impacts micro-cracking susceptibility, crystallographic texture, and residual stress distribution. The micro-cracking which is confirmed as solidification cracking occurred in high angle grain boundaries. The micro-cracking decreased progressively from ~2.50 mm/mm^2 (0° strategy) to ~0.30 mm/mm^2 (Double 90°), accompanied by improved strength-ductility synergy. The micro-cracking reduction was attributed to promotion of <100> crystallographic texture along build direction and a ~20% decrease in high angle grain boundary fraction. Post heat-treatment macro-cracking in cruciform geometry, was found to be influenced by residual stress distribution and as-built microstructure. Remelted samples with higher residual stress (808 MPa along build direction for Double 90°) exhibited severe macro-cracking (19.66 mm), whereas the 0° strategy with moderate residual stress (729 MPa along build direction) underwent minimal macro-cracking (2.15 mm). Macro-cracking in most strategies (67°, 90°, Double 67°, and Double 90°) occurred near stress concentrator notches of the cruciform, however the 0° strategy exhibited an anomalous cracking pattern, with macro-cracking occurring transverse to melt tracks at the top surface of the cruciform. This work demonstrates the critical importance of controlling residual stress formation through scan strategy optimization to obtain defect-free heat-treated CM247LC components produced by PBF–LB.

Keywords Scan strategies · Remelting · Solidification cracking · Strain age cracking · CM247LC · Residual stress · Powder bed fusion–laser beam

✉ Ahmed Fardan
fardan@chalmers.se

Jakob Schröder
Jakob.schroeder95@gmail.com

Jinghao Xu
jinghao.xu@liu.se

Håkan Brodin
hakan.brodin@siemens-energy.com

Eduard Hryha
hryha@chalmers.se

1 Department of Industrial and Materials Science, Chalmers University of Technology, Gothenburg, Sweden

2 Federal Institute For Materials Research and Testing, Berlin, Germany

3 Division of Engineering Materials, Department of Management and Engineering, Linköping University, Linköping, Sweden

4 Siemens Energy AB , Finspång, Sweden

1 Introduction

Additive manufacturing (AM), particularly powder bed fusion–laser beam (PBF–LB), is a promising technology for fabricating complex components from high-performance materials like Ni-base superalloys. These alloys, especially those strengthened by a high-volume fraction of γ′ precipitates, are critical for demanding applications such as gas turbines for aerospace and energy sectors due to their exceptional strength at high temperatures [1]. However, processing these alloys (such as CM247LC) via PBF–LB presents a significant challenge due to their high susceptibility to cracking, both micro-cracking and macro-cracking. These different forms of cracking are the reason that this alloy is classified as non-weldable which can severely compromise the mechanical integrity of the final part [2, 3].

Micro-cracking is typically attributed to a form of hot cracking (solidification or liquation cracking) that occurs during the PBF–LB process. While macro-cracking is typically attributed to a form of solid-state cracking (ductility dip or strain age cracking) that occurs during post-processing heat treatments. Solidification cracks form in the final stages of melt pool solidification when tensile stresses pull apart terminal liquid in interdendritic regions [4, 5]. Liquation cracks, on the other hand, originate from the localized melting of low-melting-point phases and segregations in the heat-affected zone (HAZ), which then tear apart under tensile stresses [4, 5]. Ductility dip cracking (DDC) is characterized by a loss of ductility over a specific temperature range, which is often promoted by limited grain boundary sliding due to the presence of precipitates like γ′ and carbides [5, 6]. This limited sliding can lead to porosity formation and, eventually, DDC. Strain age cracking (SAC) occurs due to the rapid precipitation of the γ′ phase combined with the high residual stress (RS) from the PBF–LB process [5, 7]. During heat treatment, both RS relaxation and γ′ precipitation occur. However, because the kinetics of γ′ precipitation are often faster than stress relaxation, the superposition of RS and the stresses from γ′ formation can lead to SAC [8, 9].

Different strategies have been developed that have primarily focused on minimizing micro-cracking in PBF–LB processed CM247LC. The strategies include alloy modification [10–12], nano-particle incorporation (such as TiC) [13], PBF–LB process parameter optimization (laser power, speed, hatch spacing) [14–17] and scan strategy modifications [18–21]. Alloy modification has focused on eliminating Hf along with other modifications such as including Nb (to form carbides) [10] or Al content reduction [12]. However, these compositional changes often result in alloys outside the nominal CM247LC specification, requiring extensive additional qualification testing, which limits industrial adoption. Process parameter optimization has proven to be a more viable and practical route. Early work by Carter et al. [14] indicated that moderate volumetric energy density (VED, see Eq. (2)) minimizes defects (micro-cracking and lack of fusion porosity). However, different combinations of laser power, speed, and hatch can result in the same VED but produce different defects. Therefore, linear energy density (LED, see Eq. (1)) is more suitable as it directly relates to melt pool size and shape which in turn dictates the micro-cracking behavior [15, 16]. Processing with low LED and sufficient hatch spacing has been shown to produce fine columnar < 100 > oriented grains with lower fraction of high angle grain boundaries (HAGBs) where micro-cracking occurs [15, 16].

Beyond tuning process parameters (laser power, speed, and hatch spacing), rigorous efforts have been undertaken to understand the effect of scan strategies. Carter et al. [22] showed that the island (chess board) scan strategy undergoes severe micro-cracking in overlap regions. This was confirmed by Lam et al. [18] for IN738LC, who demonstrated that island scan strategies are detrimental, producing micro-cracks in HAGBs. In contrast, bi-directional scan strategies minimize micro-cracking and produce uniform microstructure with regular columnar grains, as shown in [18, 22]. Additionally, Fardan et al. [19] demonstrated that despite using bi-directional scan strategy, stripe width also influences the micro-cracking and microstructure. This highlights that despite using identical process parameters (laser power, speed, hatch), the microstructure (and residual stress) is influenced by the scan strategy which in turn affects micro-cracking.

Recent advances in PBF–LB processing have been focused on remelting to further minimize micro-cracking [20, 23]. Liu et al. [20] performed remelting with different LED and indicated that optimized remelting (with low LED) minimizes micro-cracking due to reduction in crack susceptible HAGBs. Despite achieving samples nearly free of micro-cracks there remains a question of whether it is necessary to achieve such samples solely through intensive PBF–LB processing, or can post-processing hot isostatic pressing (HIP) be used to eliminate residual micro-cracking.

Despite successful micro-cracking mitigation routes, a critical need remains to understand how processing parameters affect residual stresses, which in turn influence macro-cracking. Hilal et al. [24] indicated that balancing micro- and macro-cracking collectively solely through PBF–LB processing is difficult. Parameters that minimize micro-cracking often produce severe macro-cracking during post-processing heat treatment, and vice versa. This behavior is hypothesized to arise from differences in RS build-up and relaxation. Additionally, Fardan et al. [16] measured low RS in samples processed with low VED. A follow-up study on scan strategies indicated that low RS result from processing with short stripe widths [19]. Therefore, understanding how different scan strategies affect RS development and macro-cracking susceptibility remains essential.

This study focuses on optimizing process parameters and subsequently studying the influence of scan rotation and remelting on micro-cracking, macro-cracking, microstructure, and mechanical performance (tensile and hardness). Although the behavior is somewhat documented for CM247LC, the novelty of this work lies in understanding how scanning strategy induced microstructure influences macro-cracking behavior. The results indicate that a holistic approach to process development is necessary, considering both micro-cracking and macro-cracking behavior.

2 Methodology

2.1 Material

Gas atomized CM247LC powder with a particle size range of 15 to 45 µm was supplied by Höganäs AB (Höganäs, Sweden). The chemical composition of the powder, as provided by the supplier, is detailed in Table 1.

2.2 Sample manufacturing

A commercial EOS M290 machine equipped with a Yb-fiber laser, with a maximum power of 400 W and a laser spot size of approximately 100 µm was used. From the previous study of the authors [16, 19], optimized parameters used higher laser power (200–300 W) and scan speed (2000–3000 mm/s) that risk melt pool instabilities. The parameter optimization was performed by varying the main parameters namely laser power (P), speed (v), hatch (h) with the layer thickness (t) being fixed at 0.03 mm. In this study, the authors studied the impact of lower power (125–150 W) and intermediate speed (1000–1600 mm/s) for a fixed hatch spacing of 0.05 mm to find optimal parameters. The parameter optimization was performed on cubes of $10 \times 10 \times 10$ mm^3 built directly on the building platform. Note: This optimization was performed using a bi-directional stripe scan strategy with interlayer scan rotation of 67° with a stripe width of 5 mm and a stripe overlap of 0.12 mm. The linear energy density (LED) and volumetric energy density (VED) is given by Eq. (1) and Eq. (2), respectively.

$$\mathrm{LED}\ \left[{}^{\mathrm{J}}\!/\!{}_{\mathrm{mm}}\right] = \frac{\mathrm{P}\ [\mathrm{W}]}{\mathrm{v}\ \left[{}^{\mathrm{mm}}\!/\!{}_{\mathrm{s}}\right]} \tag{1}$$

$$\mathrm{VED}\ \left[{}^{\mathrm{J}}\!/\!{}_{\mathrm{mm}^3}\right] = \frac{\mathrm{P}\ [\mathrm{W}]}{\mathrm{v}\ \left[{}^{\mathrm{mm}}\!/\!{}_{\mathrm{s}}\right].\ \mathrm{h}\ [\mathrm{mm}]\,.\mathrm{t}\,[\mathrm{mm}]} \tag{2}$$

The optimized parameters were then used to produce samples with five different scan strategies as shown in Fig. 1a-e. Unlike the parameter optimization, which employed a bidirectional stripe scan strategy with 67° rotation and 5 mm stripe width (stripe overlap of 0.12 mm), the five experimental scan strategies (Fig. 1a-e) were implemented without stripe scan strategy, using continuous bidirectional scanning across each layer. This difference in scan architecture represents a limitation of the present study; the optimization primarily defines a suitable LED window rather than a fully optimized parameter set for each individual scan strategy. The five strategies namely – 0°, 67°, 90°, Double 67° and Double 90° were used; where 0°, 67° and 90° is the interlayer scan rotation and 'Double' denotes the remelting performed. The remelting was done for every layer with

Table 1 Chemical composition of the CM247LC powder used in this study

	Cr	Co	Mo	C	W	Hf	Ta	Ti	Al	Zr	B	Si	O	Ni
wt%	8	9.3	0.5	0.06	9.7	1.3	3.2	0.8	5.6	0.009	0.01	0.08	0.01	Bal.

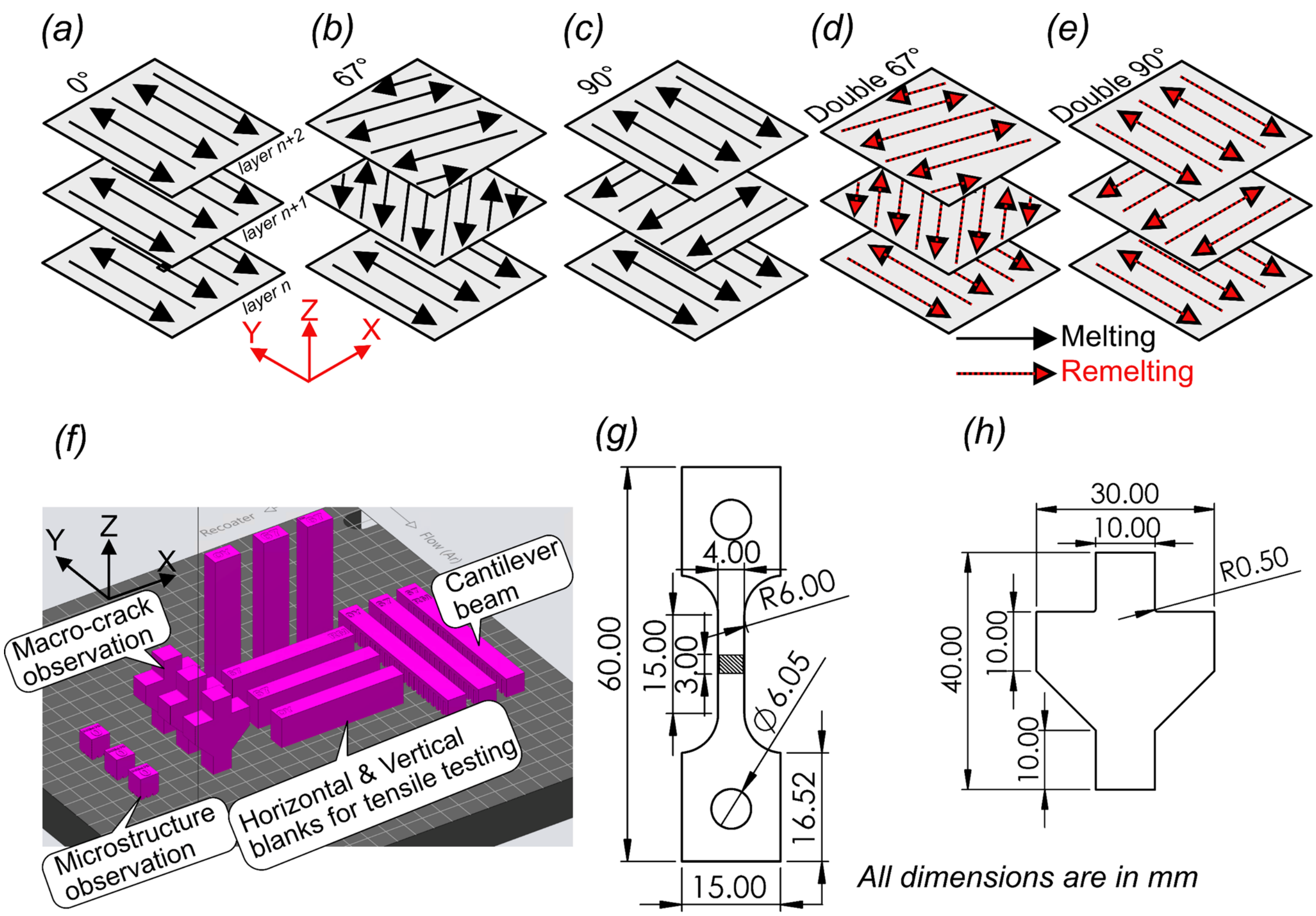

Fig. 1 Scan strategies explored in this study. Scan strategies with scan rotation of (**a**) 0°, (**b**) 67°, (**c**) 90°, (**d**) Double 67° and (**e**) Double 90°. (**f**) Schematic of the samples built for microstructure observation, cruciform for macro-cracking observation, vertical and horizontal blanks for tensile testing, (**g**) Dimensions of the tensile specimens extracted from the horizontal and vertical blanks for tensile testing, (**h**) Dimensions of the cruciform used for macro-cracking observation

the same process parameters as the first melting. These five strategies were used to produce cubes ($10 \times 10 \times 10$ mm^3), cruciform, cantilever beam, horizontal, and vertical blanks for tensile testing as shown in an over-simplified build layout in Fig. 1f. The samples were removed from the build plate using electric discharge machining (EDM).

2.3 Microstructural characterization

2.3.1 Sample preparation and defect analysis

Three cross-sections (YZ, XZ, and XY) were prepared from each 10 mm cube for microstructure observation. The samples were hot mounted in conductive bakelite resin, ground using SiC paper (from 500 to 4000 grit), and polished with diamond suspension (3 µm, using MD-Mol cloth) followed by a final 1 µm polishing step.

Defect analysis was performed on as-polished samples using Fiji ImageJ software [25] on stitched light optical microscopy (OM) images acquired at 100x magnification using Zeiss Axioscope 7. For parameter optimization, the part density was calculated by subtracting the porosity area, identified using a circularity filter (0.3 to 1.0), which effectively ignored most micro-cracks. The cracks were identified using the 'Analyze Particle' function with a circularity filter between 0 and 0.3. The major axis length of the fitted ellipse was taken as the individual crack length. Crack density was calculated as the sum of all individual crack lengths (in mm) divided by the total analyzed cross-sectional area (in mm²). This measurement was repeated three times for each sample to obtain an average value and standard deviation.

2.3.2 SEM and EBSD acquisition

A final polishing step with 0.05 µm colloidal silica was performed before SEM and EBSD acquisition using a Zeiss Gemini 450 SEM. EBSD maps were acquired at multiple magnifications (100x, 250x, and 500x) with corresponding step sizes (1 µm, 0.4 µm, and 0.2 µm). For all acquisitions, the EBSD camera was set to binning mode "Speed 2" with an exposure time of 2 ms, resulting in a hit rate of ~98–99%. Data cleaning involved removing wild spikes and zero solutions with a range of 8 to 5 nearest neighbors. The EBSD maps were processed and plotted using the MTEX toolbox (version 5.9.0) [26].

2.4 Residual stress measurements

The RS measurements were performed using a Stresstech G3 mobile diffractometer (Stresstech, Vaajakoski, Finland) operating in modified χ-mode using two position sensitive detectors (see DIN EN 15305 [27]). For all measurements, using Mn-kα radiation on the Ni-311 reflection, an acquisition time of 5 s using a 2 mm collimator was set. Before the measurements, the system was calibrated by measuring stress-free copper powder. Depth profiles were acquired by employing electrolytic layer removal using an ATM Kristall 650 polishing device (ATM Qness GmbH, Mammelzen, Germany). A 9 mm circular area of the lateral surface was electrolytically removed using a voltage of 30 V and a current of 2 A. The electropolishing solution consisted of 150 ml water, 550 ml saturated saline solution, 100 ml of ethanol, and 200 ml ethylene glycol. After each removal step, the removal depth was measured using an ID-C series 543-471B dial indicator (Mitutoyo Corporation, Kawasaki, Japan). At each removal depth 19 equidistant increments were acquired between ψ = –45 and ψ = 45°. The subsequent data analysis was performed in Xtronic using the $\sin^2\psi$ -method while assuming quasi-isotropic elastic material behavior and plane stress (i.e., $\sigma_{33}=0$). The diffraction elastic constants were calculated from the single crystal elastic constants of CM247LC [28] with ISODEC [29] using the Reuss model (s_1 = –1.436 $*10^{-6}$ MPa^{-1} and ½ s_2=6.955$*10^6$ MPa^{-1}). Residual stress relaxation due to the layer removal procedure was not considered because of the (small) size of the etched area.

The cantilever beam deflection is used to corroborate the RS measurements by XRD. The cantilever beam's geometry consisted of 20 columns. The cantilever was cut from the build plate using EDM, and its deflection was measured from the thickest column along the length at different columns using a vernier caliper. The measurement was repeated three times to obtain an average value. More information on the cantilever geometry can be found in inset of Fig. 8.

2.5 Macro-cracking observations

A cruciform geometry (shown in Fig. 1h) was used to understand the macro-cracking susceptibility of the different scan strategies. One cruciform per scan strategy was built and then underwent hot isostatic pressing (HIP) in a Quintus QIH21 URC HIP vessel with a molybdenum furnace at Quintus AB (Västerås, Sweden). The HIP was performed at a temperature of approximately 1270 °C and a pressure of 200 MPa for 4 h. Following this the cruciforms were observed in a stereo optical microscope (SOM) using Zeiss Stereo Discovery.V20. The cruciforms were then mounted, ground, polished and observed in OM as mentioned in Sect. 2.3.

2.6 Hardness and tensile measurements

Tensile properties in the as-built condition were evaluated to assess the influence of scan strategy on mechanical performance. The tensile tests were performed at a nominal strain rate of 10^{-3} s^{-1} (corresponding to 0.015 mm/s) using an Instron 5582 testing system at room temperature. The flat tensile specimens were machined using EDM as per Fig. 1g from the tensile testing blanks (horizontal and vertical) that had a dimension of 9 × 14 × 70 mm^3. The tensile specimens with a gauge length of 15 mm and a gauge width of 4 mm were prepared by EDM. The thickness of the flat specimen is 3 mm. The heat affected zone from the EDM process was removed by grinding prior to testing. An Instron 2620−601 extensometer was used to measure strains in the elastic and elasto-plastic regime (till 5%).

The macro-hardness measurements were performed on Struers DuraScan-70 G5 hardness tester using the Vickers hardness probe. The HV1 measurements were performed with a load of 1 kg, and five indents were performed in each cross-section.

3 Results

3.1 Process parameter optimization

The crack density (in mm/mm^2), density (in %) and melt pool depth (in µm) along with selected OM micrographs for PBF–LB processed CM247LC are shown in Fig. 2. It is to be noted that both LED and VED for a fixed hatch spacing increases proportionally (see Eq. (1) and Eq. (2)), therefore the results are presented in terms of LED. From Fig. 2d, it is observed that lack of fusion porosities are found when using low LED (0.08 J/mm). This is caused by the shallower and narrower melt pools which do not sufficiently overlap and can be mitigated using high LED. Figure 2f indicates however that high LED (0.15 J/mm) causes larger melt pools that sufficiently overlap, ultimately eliminating lack of fusion but increases the micro-cracking (Fig. 2a). There is a narrow optimal processing window with intermediate LED and one of the parameters set had the highest density (99.75%) and lowest crack density (0.19 mm/mm^2). This

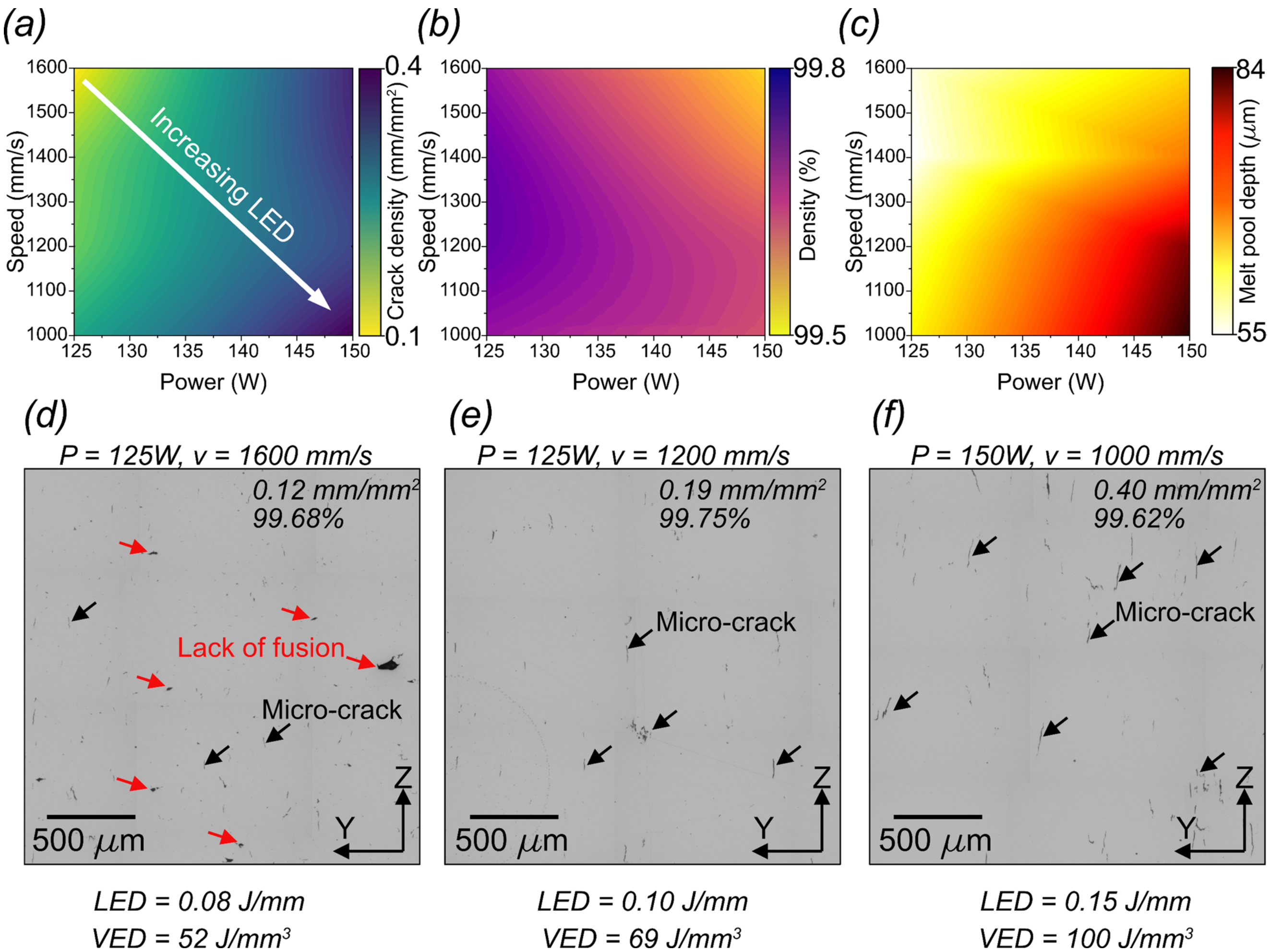

Fig. 2 Results on process optimization for the parameter used in this study. (**a**) Crack density (in mm/mm²), (**b**) Density (in %) and (**c**) Melt pool depth (in µm) obtained from image analysis. (**d**) –(**f**) selected OM micrographs indicating lack of fusion porosity and micro-cracks

Table 2 Optimized process parameter employed hereon in this study

Power (W)	Speed (mm/s)	Hatch (mm)	Layer thickness (mm)
125	1200	0.05	0.03

optimized parameter set (Table 2) is hereon used for further experiments with the different scan strategies (Fig. 1a-e).

3.2 Micro-cracking and microstructure

The micro-cracks were found to be significantly affected by the different scan strategies (Fig. 3 ***and*** Table 3). The overall trend observed is that both the scan rotations (67° and 90°) aid in minimizing the crack density, however the remelting strategies (Double 67° and Double 90°) further lowered the crack density. The 0° strategy exhibited the highest average crack density in YZ cross-section (2.52 mm/mm^2) and displayed anisotropic cracking behavior, with the XZ cross-section having lower crack density (0.49 mm/mm^2). In contrast, both the 67° and 90° scan strategies resulted in significantly lower micro-crack densities (~0.5 mm/mm^2) and a more isotropic cracking distribution across the YZ and XZ planes, demonstrating that scan rotation is an effective way to minimize this anisotropy. The most effective strategies for crack suppression were the remelting strategies, with Double 67° and Double 90° yielding the lowest overall micro-crack densities of ~0.30 mm/mm^2. Notably, the crack densities measured for the scan strategies are higher than the optimized process (0.19 mm/mm^2). This indicates that apart from the scan rotation, stripe width also has an important effect on crack density, which was shown by Fardan et al. [19].

The SEM micrographs (Fig. 4a, b) reveal evidence of dendritic solidification structure on the crack surface indicating that the micro-cracks occurred during the terminal stages of solidification. The presence of such solidification structures were observed in the literature and is a clear indicator of solidification cracking [16, 19, 30]. It is clear from Fig. 4b that the micro-cracks were found to occur in regions

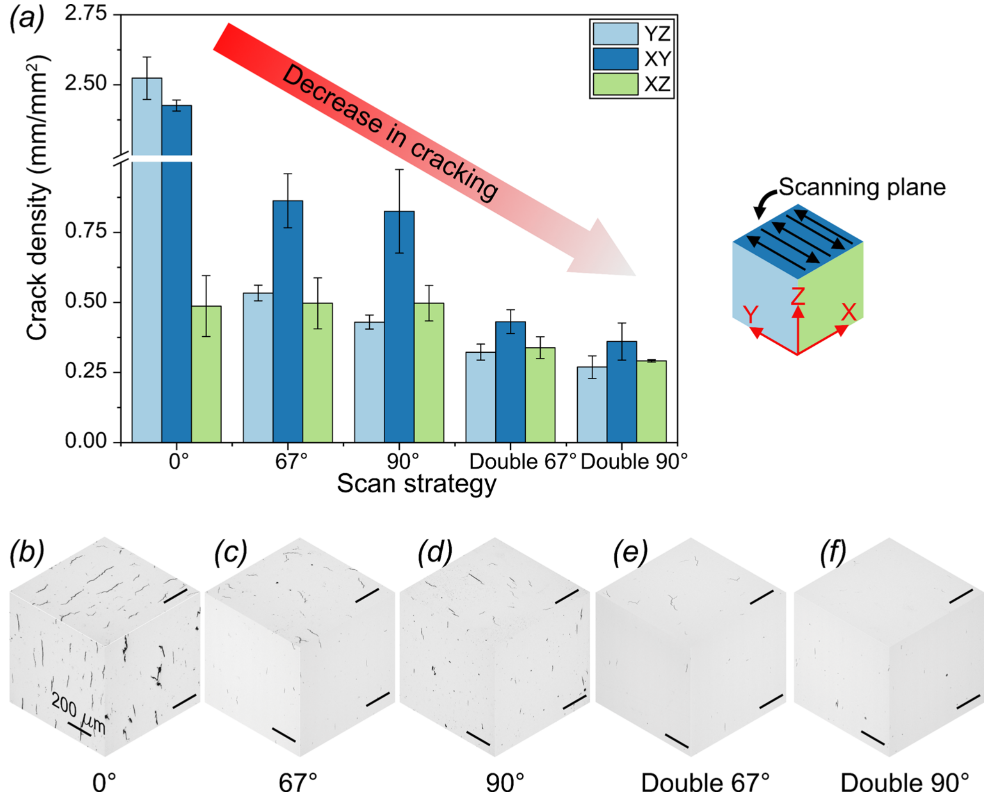

Fig. 3 (**a**) Crack density (solidification crack) measurements (in mm/mm^2) for different scanning strategies measured in three planes. Error bars correspond to the standard deviation 2σ, (**b**)-(**f**) Representative micrographs of the three cross-sections represented as a cube. The scale bar corresponds to 200 µm

Table 3 Average crack density (micro-crack) values (in mm/mm^2) obtained for the different scan strategies from the three cross-sections

Strategy	Crack density (mm/mm^2)		
	YZ	XY	XZ
0°	2.52 ± 0.08	2.43 ± 0.02	0.49 ± 0.11
67°	0.53 ± 0.03	0.86 ± 0.10	0.50 ± 0.09
90°	0.43 ± 0.03	0.83 ± 0.15	0.50 ± 0.06
Double 67°	0.32 ± 0.03	0.43 ± 0.04	0.34 ± 0.11
Double 90°	0.27 ± 0.04	0.36 ± 0.07	0.29 ± 0.02

where the direction of the primary dendrites changed, indicating that they occur at grain boundaries confirmed through EBSD (Fig. 4c, d) [31]. The maximum misorientation of the grains close to the micro-cracks (indicated in Fig. 4d) revealed that cracks occurred in high-angle grain boundaries (HAGBs) with misorientation ≥ 15°. The misorientation measurements across the micro-cracks were measured for all the scan strategies to obtain a statistical overview, which is represented as a box plot in Fig. 4e. For all scan strategies, the mean and median misorientation of the cracks is found to be between 35° and 45°. The scarcity of data points for Double 67° and Double 90° is due to the lower crack density of these processes (Fig. 3; Table 3). Nevertheless, the data confirms that for all scan strategies, the maximum misorientation of the adjacent grains with micro-cracks cracks between 35° and 50° falls between the 25th and 75th percentile.

EBSD analysis was performed to investigate the crystallographic texture for the three cross-sections for five different scan strategies. Figure 5 represents the three-dimensional cube of the IPF map along the build direction (Z) along with the respective pole figures obtained from the YZ cross-section. It is clear that all the strategies have a <100> crystallographic texture along the build direction, which is characteristic of Ni-base superalloys produced by PBF–LB [30]. However, the intensity of this texture varied significantly. The 90° scan strategy exhibited a higher <100> texture intensity (maximum MRD value of 6.86) compared to the 0° and 67° strategies (values in the range of ~ 6–6.3). Most notably, the remelting strategies (Double 67° and Double 90°) displayed the highest MRD (values of ~ 9.5), indicating that remelting further promotes the development of the <100> orientation along the build direction. The summary of the grain size, in terms of equivalent circle diameter (ECD) and fitted ellipse major diameter along with the aspect ratio is shown in Table 4 for YZ and XZ cross-sections. Comparing both the cross-sections, all the other strategies except 0° have similar grain size and aspect ratios. Notably, the remelting behavior have induced long columnar grains (max.~600–700 µm from fitted ellipse major diameter) with large aspect ratios (max. ~35). Interestingly, the grain statistics of the XZ cross-section of 0° strategy is similar to 67° except for the maximum aspect ratio. This partially explains the reason for similar

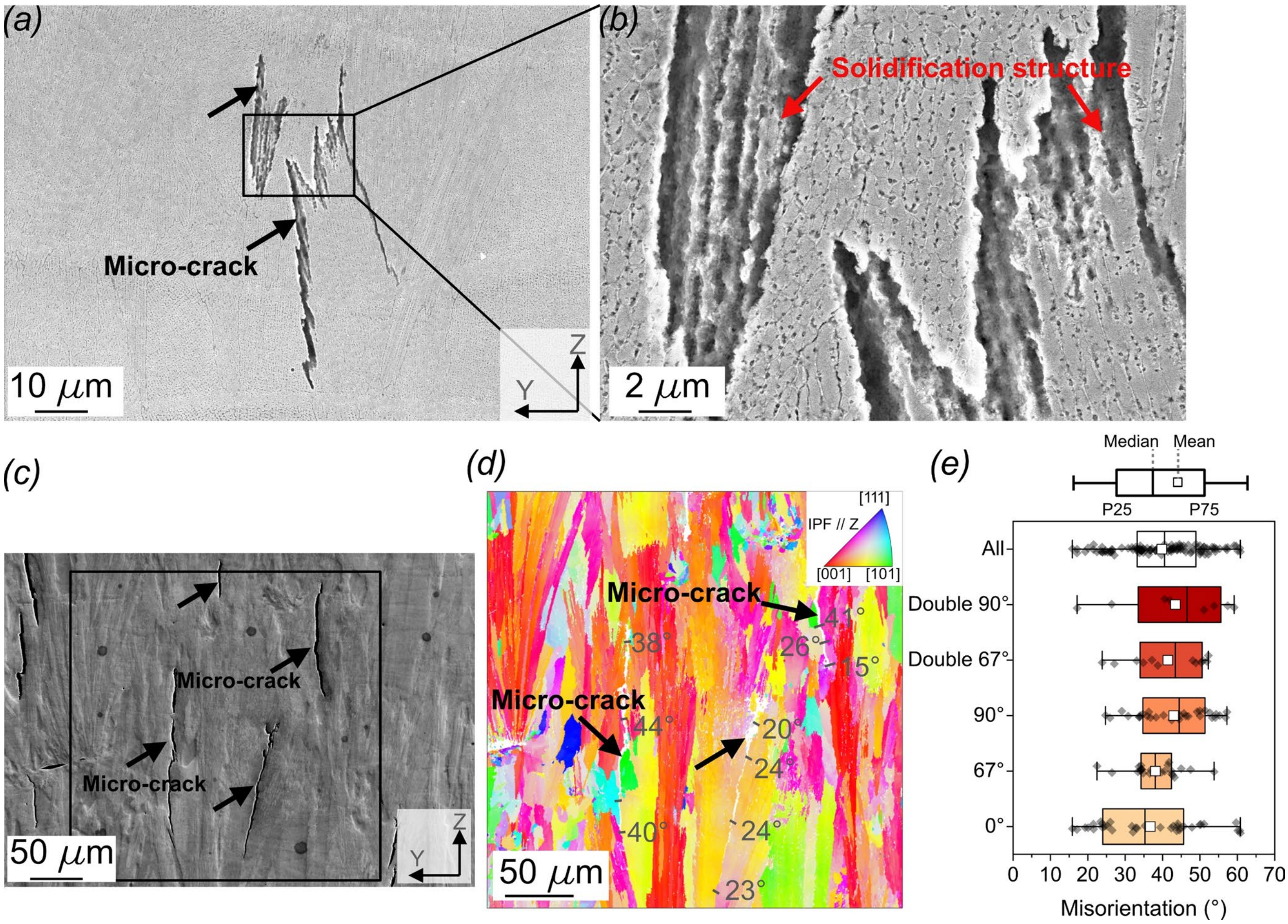

Fig. 4 (**a**), (**b**) SEM micrographs showing micro-crack and evidence of solidification structure (**c**) SEM micrograph showing micro-crack and the box indicates location of EBSD map shown in (**d**), (**d**) EBSD map in IPF representation along the build direction (Z). The maximum misorientation measured (in °) is shown in the respective locations, (**e**) The maximum misorientation in the grain boundaries containing solidification cracking for different scan strategies represented in the form of box plot

solidification crack densities for the XZ-cross section of 0°. However, the misorientation between the grains has a major role in the cracking behavior than the grain statistics (size and aspect ratio).

The reason for the increased <100> crystallographic texture for the 'Double' samples is due to the remelting causing a shallower melt pool which can be clearly observed from the top layer of the sample in Fig. 6b for Double 90°, when compared to the 90° strategy (Fig. 6a). The 90° strategy has a mix of different orientations, while the Double 90° has <100> oriented grains. This is caused due to the promotion of the epitaxial grain growth due to the shallow melt pool for the remelting strategy. The shallow melt pool is likely caused due to the lower laser absorptivity of the bulk when compared to the powder [32]. This ultimately leads to lower energy absorption by the bulk sample that forms a shallow melt pool. This shallow melt pool enables microstructure tailoring where the first exposure can be used to consolidate the material, and the remelting strategy can be used to promote the <100> oriented with minimized crack susceptible HAGBs. Although shallow melt pools can directly be obtained by lowering the LED without using remelting, there is a risk of increased lack of fusion (as shown in Fig. 1d) which is circumvented by the remelting strategy.

3.3 Residual stress

Residual stress (RS) depth profiles, measured by XRD is shown in Fig. 7. RS at the surface (0 μm depth) are minimal due to the presence of partially melted/sintered powder [16], and the RS magnitude is tensile and the magnitude increases until a depth of ~150 μm typical of PBF–LB processed alloys [33]. Along the Z-(build) direction (Fig. 7a), the lowest RS measured was 612 ± 39 MPa for the 90° scan strategy. The RS for the 0° and 67° strategies at the same depth were approximately 729 ± 93 MPa and 662 ± 56 MPa, respectively. Notably, the RS for the remelting strategies Double 67° and Double 90° were 725 ± 54 MPa and

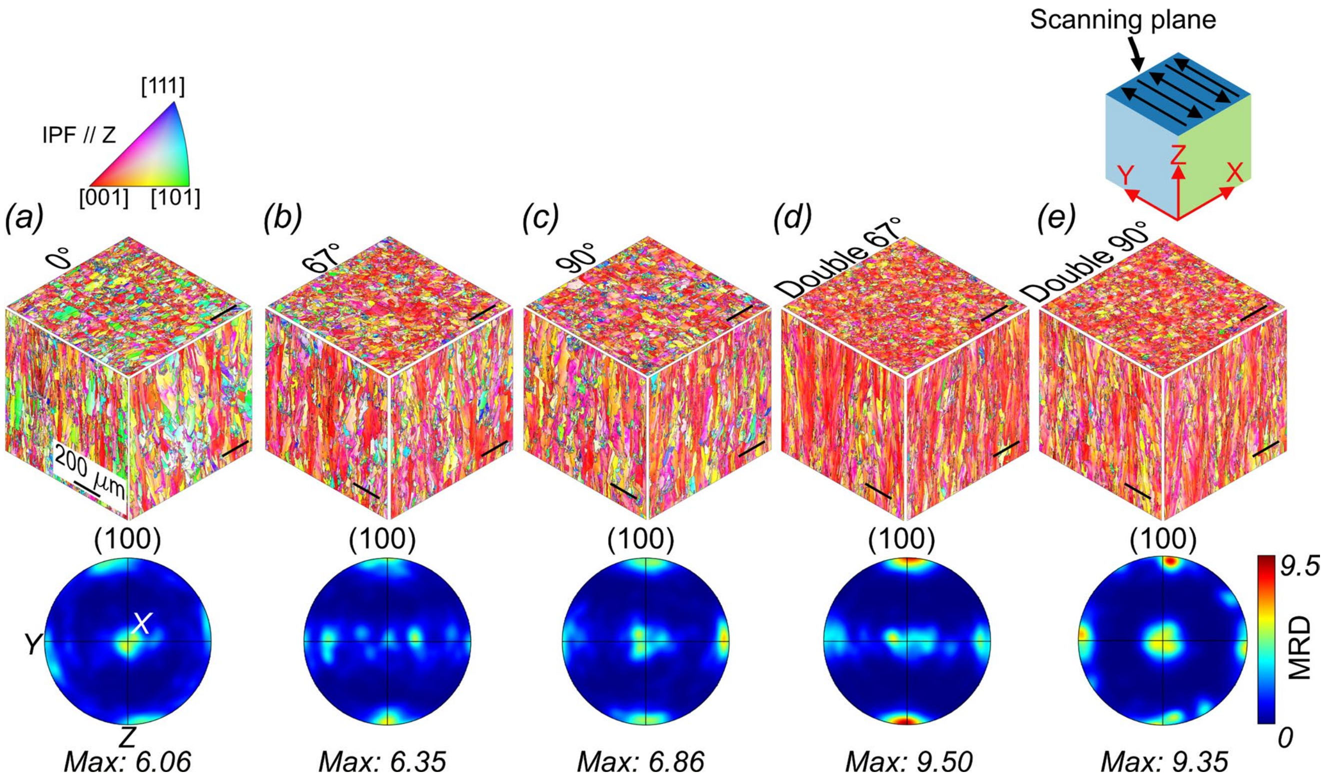

Fig. 5 EBSD orientation maps in inverse pole figure representation for different scanning strategies. The IPF coloring for each cross-section is with respect to the build direction (along Z-axis). The (100) pole figures shown are for the IPF map from YZ cross-section. The pole figure intensity is represented as multiples of random distribution (MRD) The maximum MRD from the pole figure is shown under the respective pole figures. The scale bar corresponds to 200 µm

Table 4 Summary of average and maximum grain size and grain aspect ratio obtained from the EBSD of the YZ and XZ cross-section including border grains. ECD = Equivalent circle diameter

Strategy	Average			Maximum		
	Aspect ratio	ECD (µm)	Fitted ellipse major diameter (µm)	Aspect ratio	ECD (µm)	Fitted ellipse major diameter (µm)
YZ cross-section						
0°	4.37	12.1	26.2	27.6	109.3	394.2
67°	3.95	12.5	25.7	21.2	207.8	550.0
90°	3.85	12.8	25.8	26.5	167.1	397.0
Double 67°	5.49	15.0	36.9	35.5	329.1	730.0
Double 90°	4.87	14.6	33.3	35.9	244.8	608.6
XZ cross-section						
0°	3.65	13.6	27.3	18.98	200.3	528.0
67°	4.08	13.2	27.1	24.98	210.9	525.0
90°	5.90	13.1	28.3	28.44	227.4	619.0
Double 67°	5.92	13.3	33.3	34.73	309.6	725.7
Double 90°	5.90	14.4	34.9	33.07	285.7	618.4

808 ± 97 MPa, respectively, indicating that remelting result in higher RS which is the similar behavior observed for the RS measurements along the X-direction (Fig. 7b).

The cantilever beam deflection measured across the different columns is shown in Fig. 8. The maximum deflections for the 0°, 67°, and 90° strategies were 19.45 mm, 18.29 mm, and 19.98 mm, respectively. For the remelting strategies, the deflections were 19.30 mm for Double 67° and 20.35 mm for Double 90°. From both the XRD and cantilever deflection, the layer-wise remelting leads to higher RS than the single melting. And the no scan rotation had intermediate RS levels in comparison to 67° and 90°.

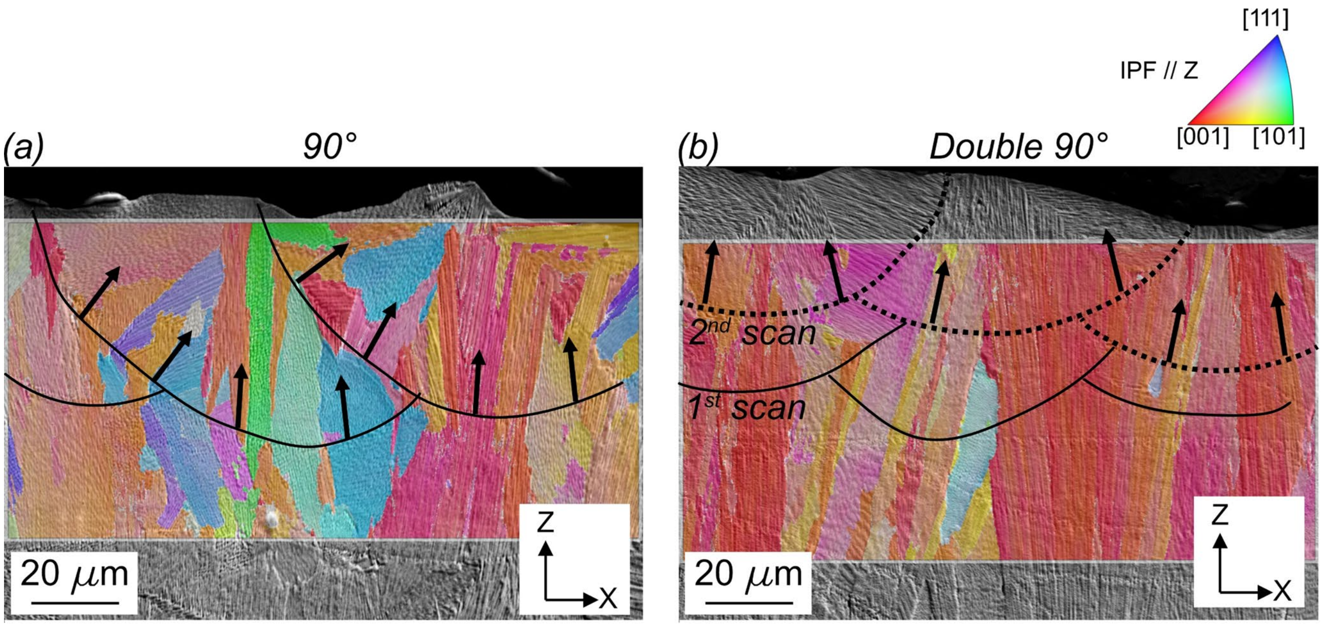

Fig. 6 EBSD orientation map in IPF representation overlayed on a slightly etched SE micrograph with melt pools outlined for (**a**) 90° scan strategy, (**b**) Double 90° scan strategy

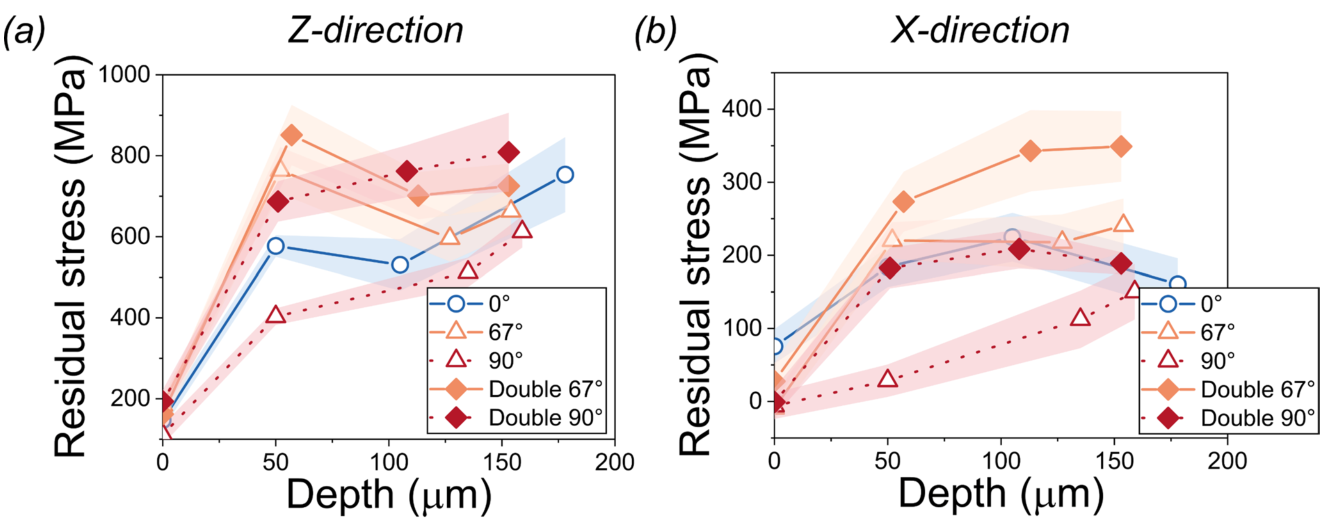

Fig. 7 Residual stress depth profiles obtained by XRD along the (**a**) Z-direction and (**b**) X-direction. Error bands correspond to the standard deviation 2σ

3.4 Macro-cracking

The macro-cracks on the cruciform samples, observed post-HIP, were analyzed using SOM from different directions, while OM was done on polished cross-section. Figure 9 indicates that macro-cracking has occurred for all the scan strategies. Interestingly, the macro-cracking for the 0° scan strategy was not found in the four designated stress concentrator notches. Instead, a crack was observed on the top of the sample in the XY plane, oriented perpendicular to the scanning direction/melt track (the scanning direction for the 0° strategy was along the Y-axis). In contrast, the other strategies primarily exhibited cracking in one or multiple notches. Both the 67° and Double 67° strategies had macro-cracking on the top-right notch. Similarly, both the 90° and Double 90° strategies had macro-cracking in the bottom notches, along with some cracks on the top surface in the XY plane.

The polished cross-sections (Figure S1) revealed additional macro-cracks that were previously not visible from the SOM. It should be noted that the top part of the 0° cruciform was sectioned and rotated to make the macro-crack visible in these micrographs. The total length of the macro-cracks measured from the polished cross-sections

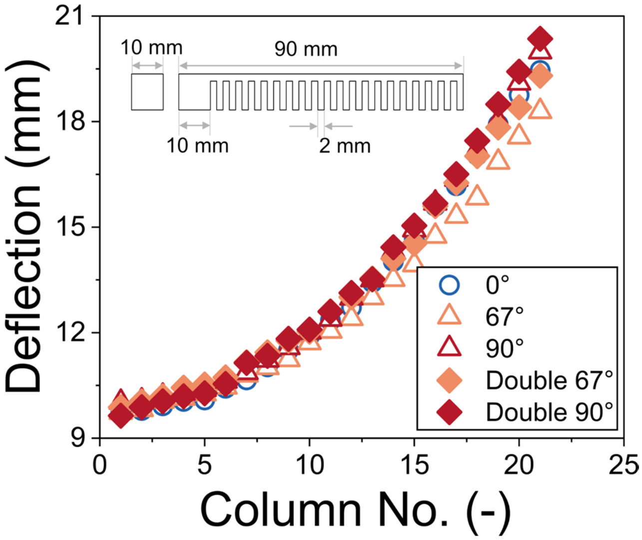

Fig. 8 Deflection of the cantilever obtained along the length

(Figure S1) is summarized in Table 5. The 0° scan strategy had the lowest total macro-cracking length (2.15 mm). The 67° and 90° strategies had crack lengths of 11.70 mm and 10.05 mm, respectively. While the double exposure reduced the crack length for the Double 67° strategy (9.06 mm), it significantly increased the crack length for the Double 90° strategy (19.66 mm).

Further observations (Figure S2) revealed that the severity of the macro-cracks was not uniform. For the 90° and Double 90° strategies, the opening of some macro-cracks on the top notches was minimal compared to other, more severe cracks that were prominently visible (even to the naked eye). These less severe macro-cracks would not have been detected without analysis of the polished cross-sections. The macro-cracks observed are clearly transgranular before crack termination, however crack initiation closer to the notch is not clear if it intergranular or transgranular. It is to be noted that the macro-crack observations reported here should be regarded as preliminary trends, since only one cruciform per scan strategy was tested. Further studies with larger sample numbers are required to statistically confirm these differences.

3.5 Mechanical response

The engineering stress-strain curves in the as-built conditions for selected strategies in vertical and horizontal direction are shown in Fig. 10 along with the summary of the tensile properties shown in Table 6. Please note that vertical direction refers to the tensile loading direction parallel to the build direction (Z), and horizontal direction refers to the tensile loading transverse to the build direction. The tensile performance of the 0° strategy is the worst in both the vertical and horizontal directions, attributed to the increased solidification cracking, as shown in Fig. 3b. The tensile performance (strength and ductility) is improved in both directions when scan rotation (67° or 90°) is employed (Table 6). Further improvement in tensile performance is achieved with remelting strategies (Double 67° or Double 90°). The improvement in strength and ductility with scan rotation and remelting strategies align with the reduced solidification crack density observed (Fig. 3). Additionally, the hardness measurements (HV1) also indicate a similar behavior with increasing hardness in the following manner no scan rotation < scan rotation < remelting, correlating with the tensile test results.

4 Discussion

The results of this study demonstrate a complex relationship between scan strategy, microstructure, residual stresses, micro-cracking (identified as solidification cracking), macro-cracking and mechanical properties in PBF–LB processed CM247LC superalloy. This work demonstrates that process parameters and scan strategies tuned to suppress solidification cracking do not necessarily result in reduced macro-cracking, emphasizing the need for the importance of holistic approach to process development.

The melt pool geometry (size and shape) and scan strategies shown here and elsewhere [15, 16, 19, 20] are known to affect the orientation of the primary dendrite growth and, in turn, the microstructure. The melt pool geometry is influenced primarily by varying the energy input (LED) which correlates well with both the melt pool depth and solidification cracking, as shown by both Grange et al. [15] and Fardan et al. [16]. It is demonstrated that a narrow optimal processing window (with minimal defects) exists for CM247LC: low LED leads to lack of fusion porosity due to shallow and narrow melt pools that do not sufficiently overlap, whereas high LED causes deep and wide melt pools that eliminate lack of fusion but increase solidification cracking, agreeing with the literature [16, 34]. Low LED combined with small hatch spacing promotes the <100>-oriented columnar grains along the build (Z) direction with a lower fraction of HAGBs, the sites where solidification cracks occur [15, 16]. The solidification cracking occurs due to the insufficient liquid feeding during the terminal stages of solidification. By tailoring the processing to produce smaller melt pools, the melted volume is reduced, resulting in lower shrinkage strains (and associated stresses) upon solidification. This finding aligns with the simulation results by Dye et al. [35]. for welding of IN718, where it was indicated that processing with low LED is beneficial as it minimizes the tensile stress in the mushy zone.

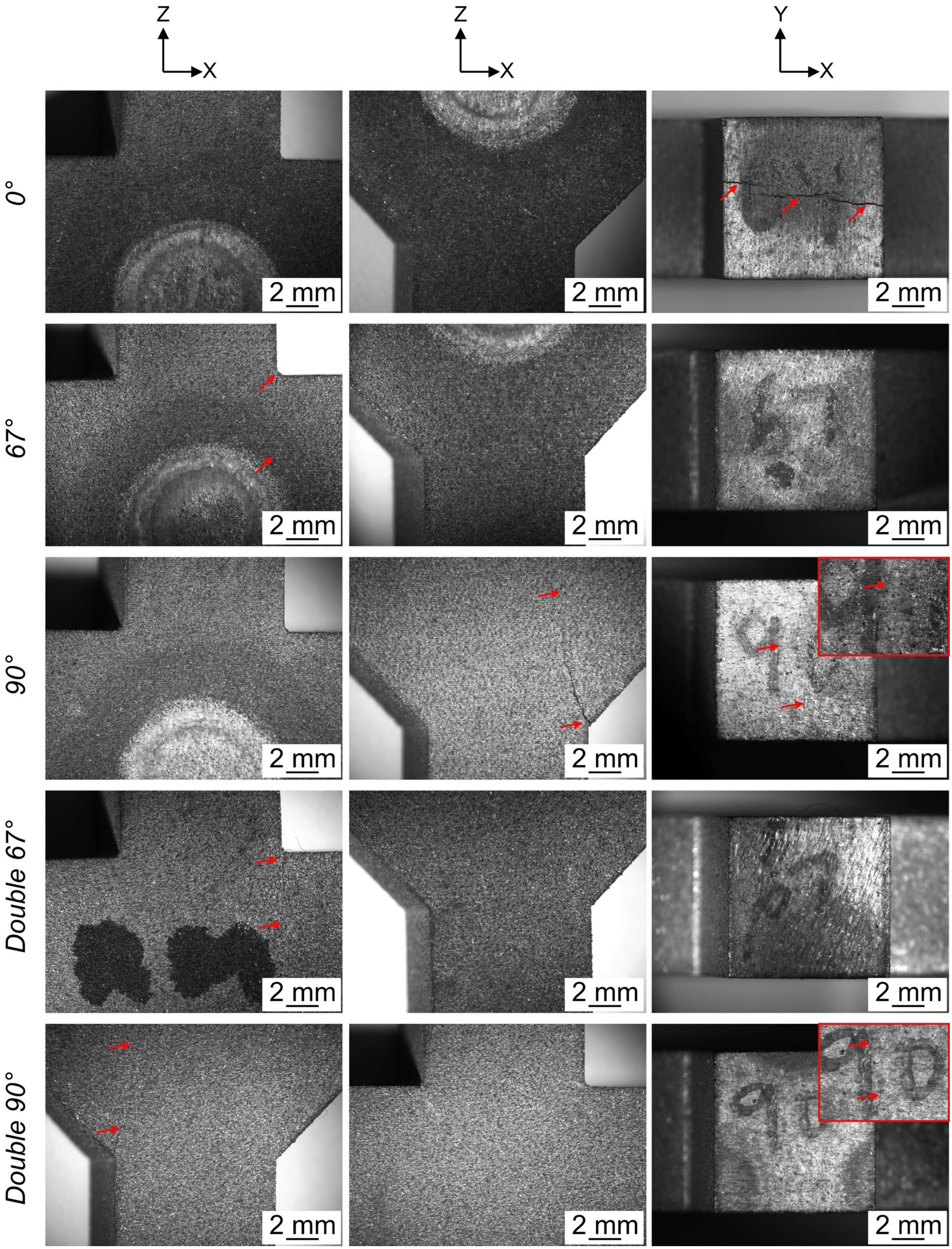

Fig. 9 Stereo Optical Microscope (SOM) micrographs of the cruciforms after HIP. Red arrows indicate the macro-cracks

Table 5 Total length of macro-cracks (in mm) measured on a polished cross-section of the cruciforms manufactured with different scan strategies post-HIP

Strategy	0°	67°	90°	Double 67°	Double 90°
Σ Crack length (mm)	2.15	11.70	10.05	9.06	19.66

Table 6 Summary of the tensile and hardness (HV1) results. YS = Yield strength, UTS = Ultimate tensile strength

Strategy	YS (MPa)	UTS (MPa)	Elongation (%)	Vickers hardness (HV1)
Vertical direction				
0°	751 ± 21	1168 ± 5	25.1 ± 1.3	400 ± 21
67°	791 ± 21	1218 ± 18	24.5 ± 4.7	408 ± 10
90°	820 ± 11	1210 ± 6	22.3 ± 0.2	409 ± 10
Double 67°	817 ± 18	1259 ± 12	26.6 ± 2.5	440 ± 5
Double 90°	860 ± 10	1245 ± 10	29.2 ± 2.0	441 ± 10
	YS (MPa)	UTS (MPa)	Elongation (%)	HV1
Horizontal direction				
0°	802 ± 7	1141 ± 9	13.3 ± 0.4	388 ± 13
67°	883 ± 7	1179 ± 7	14.4 ± 0.5	402 ± 15
90°	876 ± 4	1200 ± 3	15.8 ± 0.2	421 ± 9
Double 67°	919 ± 2	1242 ± 4	14.9 ± 2.1	418 ± 9
Double 90°	925 ± 15	1255 ± 5	14.9 ± 1.0	439 ± 12

The solidification cracking in PBF–LB processed CM247LC occurs predominantly in the transverse direction to the melt track, as evident for the no scan rotation strategy (0°) (Fig. 3a). This observation aligns with the findings by Cloots et al. [36] and Grange et al. [15] for PBF–LB processed IN738LC. In contrast, solidification cracks in welding are reported to occur in the longitudinal direction of the weld/melt track [37]. This fundamental difference arises from the distinct RS distributions and microstructure development in the two processes. In welding, the mushy zone extends longitudinally and the transverse tensile stresses normal to the weld axis leads to cracks that propagate along the centerline of the weld/melt track [35]. In contrast, PBF–LB processing involves layer-by-layer melting that produces columnar grains that grow epitaxially along the build direction with HAGBs distributed perpendicular to the scan direction (Y-direction) (Fig. 5a). Critically, RS development in PBF–LB is dictated by scan rotation strategy. Serrano-Munoz et al. [38] demonstrated that IN718 samples processed by PBF–LB with no scan rotation exhibit the highest RS perpendicular to the melt tracks (Y-direction). This combination of high RS and long columnar grains with misorientation angles ≥ 15° oriented perpendicular to the scan direction leads to the high solidification crack density observed in the YZ cross-section (Table 3).

The observed reduction in solidification cracking with scan rotation and remelting is a direct consequence of controlling grain boundary character, manifested in a reduction of HAGB fraction (Table 7). With scan rotation (67° or 90°), the HAGB fraction (misorientation > 15°) decreases to ~45%, compared to 52.5% for 0° strategy. Remelting strategies achieve further reduction of ~30% through epitaxial growth promoted by the shallower melt pools of the second exposure. Notably, grain size statistics (Table 4) show no correlation with solidification cracking behavior, whereas grain boundary misorientation shows excellent correlation. This observation is consistent with Wang et al. [39], who established that a minimum misorientation of 13° is required for solidification cracking. The present study indicates that

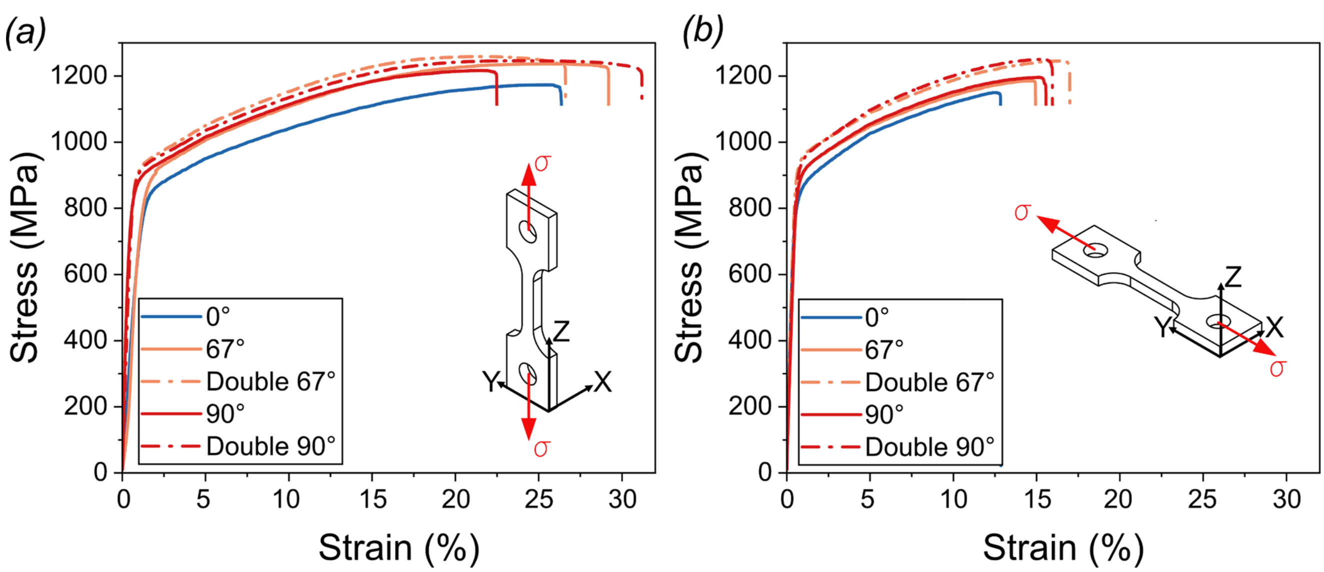

Fig. 10 Representative engineering stress-strain curves for CM247LC in as-built condition printed with different scan strategies for (a) vertical direction and (b) horizontal direction. Please note vertical direction refers to the loading along the build direction (Z) and horizontal direction refers to the loading transverse to the build direction

Table 7 HAGB fraction (in %) obtained from EBSD map. HAGB is defined with misorientation ≥ 15°

Strategy	HAGB fraction (%)	
	YZ	XZ
0°	52.5	67.1
67°	44.4	48.0
90°	45.0	47.4
Double 67°	28.3	31.5
Double 90°	35.0	31.0

solidification cracks preferentially occur at grain boundaries with misorientation ≥ 15–20°, suggesting a higher critical threshold than reported in conventional welding literature. This highlights that grain boundary misorientation, rather than grain size, is the primary microstructural factor controlling solidification cracking susceptibility.

The macro-cracking observed in the cruciform is attributed to solid-state cracking mechanisms which can be subdivided into SAC and DDC that have been reported previously in [24, 40, 41]. However, it is more likely that SAC is the dominant mechanism in CM247LC, which is caused by the rapid γ′ precipitation before relaxing the RS from the PBF–LB process [41]. Precipitation of γ′ is known to occur rapidly in medium to high γ′ strengthened alloys at temperatures above ~700–800 °C, with precipitation occurring within minutes (demonstrated for IN738LC [42]). During this critical window, the combined stress (RS from PBF–LB + γ′ precipitation induced stresses) may exceed the grain boundary cohesive strength, particularly at high angle grain boundaries leading to SAC [41]. However, the SAC observed in the cruciform exhibits a intergranular cracking (***Figure S2***), with unclear crack propagation near the notch and then transitioning to intergranular away from the notch. This difference in SAC behavior is attributed to the differences in local RS, which is significantly higher near the notches [43]. The high RS near the notch, combined with γ′ precipitation induced stresses, can lead to significant crack opening observed near the notch. Apart from SAC, contributions from DDC or mixed crack mechanisms could not be excluded based on the current evidence. A definitive separation of SAC and DDC would require time-resolved or local-strain/precipitation measurements, which are beyond the scope of this study.

Remelting strategies exhibit longer macro-cracks (19.66 mm for Double 90°, Table 5) due to columnar grain structure (Table 4: 600–730 µm maximum grain length, aspect ratio ~ 35). Since macro-cracks propagates along intergranular paths (Figure S2), the elongated columnar grains provide extended grain boundary crack propagation routes. Combined with higher residual stresses in remelted samples (808 ± 97 MPa for Double 90° vs. 612 ± 39 MPa for 90°, Fig. 7a), this explains why remelted samples show the longest macro-crack despite minimal solidification cracking.

However, Double 67° despite having similar columnar grain structure to Double 90° had macro-crack length similar to 67° strategy, despite Double 67° having higher RS levels than 67°. This is an interesting observation and requires further study, perhaps by mapping RS distribution closer to the notches using synchrotron X-ray or neutron diffraction techniques.

Additionally, macro-crack did not occur near the notch but on the top of the cruciform, indicating a difference in cracking mechanism than the scan rotation and remelting strategies. Interestingly both micro-cracking and macro-cracking occurred transverse to the scan direction for the 0° strategy. It is noted that the RS results in both Z and X-direction were comparable for the 0° strategy in comparison to the other strategies (67° or 90°) (Fig. 7a, b). However, from literature [38], the highest RS for the 0° strategy is in the Y-direction (not measured in this study). This high RS transverse to the columnar grains (YZ cross-section, Fig. 5a) leads to the lower macro-cracking observed for the no scan rotation strategy.

Overall, there is a critical need for improved understanding of RS distribution, especially near stress concentration notches, to reduce macro-cracking susceptibility in PBF–LB CM247LC components. Significant efforts have been directed toward minimizing solidification cracking through process optimization [20, 21], which can be effectively mitigated using hot isostatic pressing [44, 45]. However, macro-cracking remains a persistent challenge that cannot be entirely eliminated through post-processing alone. Therefore, future efforts must focus on minimizing macro-cracking through an integrated approach combining PBF–LB process optimization, post-processing heat treatment, and alloy design strategies.

5 Conclusions

The following are the main conclusions drawn from the study:

- Both scan rotation and remelting effectively reduce solidification cracking in PBF–LB processed CM247LC. The double exposure strategies (Double 67° and Double 90°) resulted in the lowest crack densities (~0.3 mm/mm^2), representing an order-of-magnitude reduction compared to the 0° strategy (~2.50 mm/mm^2).
- All scan strategies produce strong <100> crystallographic texture along the build direction, with remelting strategies exhibiting higher texture intensity (maximum ~9.5) compared to single exposure strategies (~6). This enhanced texture correlates with reduced HAGB fraction (from ~ 50% for 0° to 30% for remelting strategies).

- Grain boundary misorientation influences the solidification cracking more than the grain size or aspect ratio.
- Solidification cracks are predominantly found along HAGBs with misorientation angles between 35° and 50° for all strategies except for no scan rotation strategy (0°), which had cracks at HAGBs with misorientation as low as 15°.
- A complex relationship exists between (micro) solidification cracking, residual stress and the presented preliminary macro-cracking results. Strategy with high solidification cracking (0° strategy) exhibited lowest macro-cracking (2.15 mm total crack length), whereas nearly solidification crack free sample for both scan rotation (67 or 90°) and remelting (Double 67° or Double 90°) showed severe macro-cracking (~10–20 mm).
- The preliminary macro-cracking observations in all the strategies occurred in the bottom or top notch of the cruciform except for the 0° strategy that occurred on the top of the cruciform transverse to the scan direction. This difference in behavior is attributed to the difference in residual stress accumulation.

Supplementary Information The online version contains supplementary material available at https://doi.org/10.1007/s40964-026-01701-z.

Acknowledgements This work has been performed in the framework of MAGDA (Materials for green hydrogen fueled gas turbines through additive manufacturing) project, TILDA (Tailored microstructure control by Additive Manufacturing as enabler for green hydrogen fueled gas turbines) project and the Centre for Additive Manufacturing – Metal (CAM2), all supported by Sweden's Innovation Agency (Vinnova).

Author contributions Ahmed Fardan: Conceptualization, Investigation, Visualization, Writing – original draft, Writing – review & editing. Jakob Schröder: Investigation, Visualization, Writing – review & editing. Jinghao Xu: Investigation, Visualization, Writing – review & editing. Håkan Brodin: Conceptualization, Supervision, Writing – review & editing. Eduard Hryha: Conceptualization, Supervision, Writing – review & editing, Funding acquisition.

Funding Open access funding provided by Chalmers University of Technology.

Data availability The data that supports the findings of this paper are available from the authors on reasonable request.

Declarations

Conflict of interest The authors declare that they have no known competing financial interests or personal relationships that could have appeared to influence the work reported in this paper.

References

1. Sanchez S, Smith P, Xu Z, Gaspard G, Hyde CJ, Wits WW, Ashcroft IA, Chen H, Clare AT (2021) Powder Bed Fusion of nickel-based superalloys: a review. Int J Mach Tools Manuf 165:103729. https://doi.org/10.1016/j.ijmachtools.2021.103729
2. Adegoke O, Andersson J, Brodin H, Pederson R (2020) Review of laser powder bed fusion of gamma-prime-strengthened nickel-based superalloys. Met (Basel) 10:1–26. https://doi.org/10.3390/met10080996
3. Enrique PD, Minasyan T, Toyserkani E (2025) Laser powder bed fusion of difficult-to-print γ′ Ni-based superalloys: A review of processing approaches, properties, and remaining challenges. Addit Manuf 106:104811. https://doi.org/10.1016/j.addma.2025.104811
4. Kou S (2003) Welding metallurgy, 2 edn. Wiley
5. DuPont JN, Lippold JC, Kiser SD (2009) Welding metallurgy and weldability of nickel-base alloys. Wiley Online Library. https://doi.org/10.1002/9780470500262
6. Rhines FN, Wray PJ (1961) Investigation of the intermediate temperature ductility minimum in metals. ASM TRANS Q 54:117–128
7. Mercelis P, Kruth JP (2006) Residual stresses in selective laser sintering and selective laser melting. Rapid Prototyp J 12:254–265. https://doi.org/10.1108/13552540610707013
8. Xu J, Kontis P, Peng RL, Moverare J (2022) Modelling of additive manufacturability of nickel-based superalloys for laser powder bed fusion. Acta Mater 240:118307. https://doi.org/10.1016/j.actamat.2022.118307
9. Donachie MJ, Donachie SJ (2002) Superalloys: a technical guide., 2. ed., ASM
10. Markanday JFS, Christofidou KA, Miller JR, Livera ER, Jones NG, Pickering EJ, Li W, Pardhi Y, Jones CN, Stone HJ (2023) The microstructural evolution of CM247LC manufactured through laser powder bed fusion. Metall Mater Trans Phys Metall Mater Sci. https://doi.org/10.1007/s11661-022-06939-0
11. Griffiths S, Ghasemi Tabasi H, Ivas T, Maeder X, De Luca A, Zweiacker K, Wróbel R, Jhabvala J, Logé RE, Leinenbach C (2020) Combining alloy and process modification for micro-crack mitigation in an additively manufactured Ni-base superalloy. Addit Manuf 36. https://doi.org/10.1016/j.addma.2020.101443
12. Hu P, Liu Z, Chen M, Li Y, Qi X, Xie J (2024) Reducing cracking sensitivity of CM247LC processed via laser powder bed fusion through composition modification. J Mater Res Technol 29:3074–3088. https://doi.org/10.1016/j.jmrt.2024.02.082
13. Büßenschütt K, Pontoreau M, Haase C, Schleifenbaum J-H (2025) Mitigation of cracks in high-performance nickel-based superalloys in powder bed fusion laser beam of metals using a metal matrix composite approach. Adv Eng Mater n/a 2500581. https://doi.org/10.1002/adem.202500581
14. Carter LN, Attallah MM, Reed RC (2012) Laser powder bed fabrication of nickel-base superalloys: influence of parameters; characterisation, quantification and mitigation of cracking. Proc

Int Symp Superalloys 577–586. https://doi.org/10.7449/2012/superalloys_2012_577_586
15. Grange D, Bartout JD, Macquaire B, Colin C (2020) Processing a non-weldable nickel-base superalloy by selective laser melting: role of the shape and size of the melt pools on solidification cracking. Materialia 12. https://doi.org/10.1016/j.mtla.2020.100686
16. Fardan A, Fazi A, Peng RL, Mishurova T, Thuvander M, Bruno G, Brodin H, Hryha E (2024) Fine-Tuning Melt Pools and Microstructures: Taming Cracks in Powder Bed fusion–laser Beam of a non-weldable Ni-base Superalloy. Materialia 102059. https://doi.org/10.1016/j.mtla.2024.102059
17. Kumar B, Sahu S, Srinivasan D, Balila NJ (2022) Influence of heat input on solidification cracking in additively manufactured CM247LC Ni-based superalloy. Metall Mater Trans A. https://doi.org/10.1007/s11661-023-07027-7
18. Lam MC, Lim SCV, Song H, Zhu Y, Wu X, Huang A (2022) Scanning strategy induced cracking and anisotropic weakening in grain texture of additively manufactured superalloys. Addit Manuf 52:102660. https://doi.org/10.1016/j.addma.2022.102660
19. Fardan A, Fazi A, Schröder J, Mishurova T, Deckers T, Bruno G, Thuvander M, Markström A, Brodin H, Hryha E (2025) Microstructure tailoring for crack mitigation in CM247LC manufactured by powder bed fusion–laser beam. Addit Manuf 99. https://doi.org/10.1016/j.addma.2025.104672
20. Liu L, Wang D, Deng G, Han C, Zhou H, Tan C, Long Y, Liu Z, Zhang M, Yang C, Yang Y (2024) Crack inhibition and mechanical property enhancement of a CM247LC alloy fabricated by laser powder bed fusion through remelting strategy. Mater Charact 214:114073. https://doi.org/10.1016/j.matchar.2024.114073
21. Liu L, Wang D, Deng G, Liu Z, Tan C, Zhou X, Han C, Jiang R, Yang Y (2023) Crack inhibition to enhance strength-ductility of CM247LC alloy fabricated by laser powder bed fusion. Mater Sci Eng A 875:145114. https://doi.org/10.1016/j.msea.2023.145114
22. Carter LN, Martin C, Withers PJ, Attallah MM (2014) The influence of the laser scan strategy on grain structure and cracking behaviour in SLM powder-bed fabricated nickel superalloy. J Alloys Compd 615:338–347. https://doi.org/10.1016/j.jallcom.2014.06.172
23. Wang Q, Zhang W, Gao P, Wang L, Chang G, Cai B, Liu C, Duan M, Peng Y, Wang K (2025) Crack healing and strength-ductility enhancement of CM247LC alloy via laser powder bed re-melting followed by hot isostatic pressing and heat treatment. Mater Charact 225:115195. https://doi.org/10.1016/j.matchar.2025.115195
24. Hilal H, Lancaster R, Stapleton D, Baxter G (2019) Investigating the influence of process parameters on the structural integrity of an additively manufactured nickel-based superalloy. Met (Basel) 9. https://doi.org/10.3390/met9111191
25. Schindelin J, Arganda-Carreras I, Frise E, Kaynig V, Longair M, Pietzsch T, Preibisch S, Rueden C, Saalfeld S, Schmid B, Tinevez J-Y, White DJ, Hartenstein V, Eliceiri K, Tomancak P, Cardona A (2012) Fiji: an open-source platform for biological-image analysis. Nat Methods 9:676–682. https://doi.org/10.1038/nmeth.2019
26. Bachmann F, Hielscher R, Schaeben H (2010) Texture Analysis with MTEX–free and open source software toolbox, Solid State Phenom. 160 294–306.
27. DIN - Deutsches Institut für Normung (2009) DIN EN 15305:2009-01, Non-destructive testing – X-ray diffraction test method for the determination of residual stresses
28. Ma S, Rangaswamy P, Majumdar BS (2003) Microstress evolution during in situ loading of a superalloy containing high volume fraction of γ′ phase. Scr Mater 48:525–530. https://doi.org/10.1016/S1359-6462(02)00504-3
29. Gnäupel-Herold T (2012) ISODEC: software for calculating diffraction elastic constants. J Appl Crystallogr 45:573–574. https://doi.org/10.1107/S0021889812014252
30. Tang YT, Panwisawas C, Ghoussoub JN, Gong Y, Clark JWG, Németh AAN, McCartney DG, Reed RC (2021) Alloys-by-design: application to new superalloys for additive manufacturing. Acta Mater 202:417–436. https://doi.org/10.1016/j.actamat.2020.09.023
31. Hariharan A, Lu L, Risse J, Kostka A, Gault B, Jägle EA, Raabe D (2019) Misorientation-dependent solute enrichment at interfaces and its contribution to defect formation mechanisms during laser additive manufacturing of superalloys. Phys Rev Mater 3:123602. https://doi.org/10.1103/PhysRevMaterials.3.123602
32. Kromer R, Gorny C, Gruhier E, Le Guen E, Arvieu C, Lacoste E (2023) Absorptivity measurement of solid and powder bed under IR laser beam. Opt Laser Technol 157. https://doi.org/10.1016/j.optlastec.2022.108508
33. Schröder J, Evans A, Luzin V, Abreu Faria G, Degener S, Polatidis E, Čapek J, Kromm A, Dovzhenko G, Bruno G, Keckes J (2023) Texture-based residual stress analysis of laser powder bed fused Inconel 718 parts. J Appl Crystallogr 56:1076–1090. https://doi.org/10.1107/S1600576723004855
34. Phan MAL, Dew O, Todd I (2024) Predictive process diagram for parameters selection in laser powder bed fusion to achieve high-density and low-cracking built parts. Addit Manuf 85:104145. https://doi.org/10.1016/j.addma.2024.104145
35. Dye D, Hunziker O, Reed RC (2001) Numerical analysis of the weldability of superalloys. Acta Mater 49:683–697. https://doi.org/10.1016/S1359-6454(00)00361-X
36. Cloots M, Uggowitzer PJ, Wegener K (2016) Investigations on the microstructure and crack formation of IN738LC samples processed by selective laser melting using Gaussian and doughnut profiles. Mater Des 89:770–784. https://doi.org/10.1016/j.matdes.2015.10.027
37. Böllinghaus T, Herold H, Cross CE, Lippold JC (2008) Hot Cracking Phenomena in Welds II. Springer. https://doi.org/10.1007/978-3-540-78628-3. https://doi.org/
38. Serrano-Munoz I, Mishurova T, Thiede T, Sprengel M, Kromm A, Nadammal N, Nolze G, Saliwan-Neumann R, Evans A, Bruno G (2020) The residual stress in as-built laser powder bed fusion IN718 alloy as a consequence of the scanning strategy induced microstructure. Sci Rep 10:1–15. https://doi.org/10.1038/s41598-020-71112-9
39. Wang N, Mokadem S, Rappaz M, Kurz W (2004) Solidification cracking of superalloy single- and bi-crystals. Acta Mater 52:3173–3182. https://doi.org/10.1016/j.actamat.2004.03.047
40. Fardan A, Gårdstam J, Brodin H, Hryha E (2024) Overcoming strain age cracking. an additively manufactured non-weldable Ni-Base superalloy through HIP, in: Eur. 2024. EPMA, Malmö. https://doi.org/10.59499/EP246281533.
41. Markanday JFS, D'Souza N, Church NL, Miller JR, Pitchforth JJC, Connor LD, Michalik S, Roebuck B, Jones NG, Christofidou KA, Stone HJ (2024) The relationship between strain-age cracking and the evolution of γ′ in laser powder-bed-fusion processed Ni-Based Superalloys. In: Cormier J, Edmonds I, Forsik S, Kontis P, O'Connell C, Smith T, Suzuki A, Tin S, Zhang J (eds) Superalloys 2024. Springer Nature Switzerland, Cham, pp 822–835
42. Schulz F, Lindgren K, Xu J, Hryha E (2024) Gamma prime formation in nickel-based superalloy IN738LC manufactured by laser powder bed fusion. Mater Today Commun 38:107905. https://doi.org/10.1016/j.mtcomm.2023.107905
43. Safizadeh S, Wuthrich R, Kwok TH (2025) Stress and crack analysis in PBF-LB IN738 with heat treatment. Int J Adv Manuf Technol 139:2073–2086. https://doi.org/10.1007/s00170-025-16016-6
44. Fardan A, Gårdstam J, Oscarsson E, Brodin H, Hryha E (2025) Impact of Hot Isostatic Pressing on Microstructure Evolution and Creep Performance of Powder Bed Fusion–Laser Beam

Processed CM247LC. Adv Eng Mater. https://doi.org/10.1002/adem.202500691
45. Bassini E, Sivo A, Martelli PA, Rajczak E, Marchese G, Calignano F, Biamino S, Ugues D (2022) Effects of the solution and first aging treatment applied to as-built and post-HIP CM247 produced via laser powder bed fusion (LPBF). J Alloys Compd 905:164213. https://doi.org/10.1016/j.jallcom.2022.164213